Revisiting the Local Leo Cold Cloud and Revised Constraints on the Local Hot Bubble

S. L. Snowden, C. Heiles, Dimitra Koutroumpa, K. D. Kuntz, Rosine Lallement, D. Mccammon, J. E. G. Peek

The Astrophysical Journal, 806:119 (12pp), 2015 June 10 doi:10.1088/0004-637X/806/1/119

REVISITING THE LOCAL LEO COLD CLOUD AND REVISED CONSTRAINTS ON THE LOCAL HOT BUBBLE

S. L. Snowden[1], C. Heiles[2], D. Koutroumpa[3], K. D. Kuntz[4], R. Lallement[5], D. McCammon[6], and J. E. G. Peek[7]
[1] NASA/Goddard Space Flight Center, Greenbelt, MD 20771, USA
[2] University of California–Berkeley, Astronomy Department, Berkeley, CA 94720-0001, USA
[3] Université Versailles St-Quentin; Sorbonne Universités, UPMC Univ. Paris 06; CNRS/INSU, LATMOS-IPSL, 11 Boulevard d'Alembert, F-78280, Guyancourt, France
[4] The Johns Hopkins University, The Henry A. Rowland Department of Physics and Astronomy, Baltimore, MD 21218, USA
[5] GEPI, Observatoire de Paris, CNRS UMR8111, Université Paris Diderot, 5 Place Jules Janssen, F-92190 Meudon, France
[6] University of Wisconsin–Madison, Department of Physics, 1150 University Avenue, Madison, WI 53706, USA
[7] Space Telescope Science Institute, 3700 San Martin Drive, Baltimore, MD 21210, USA
Received 2015 January 16; accepted 2015 April 22; published 2015 June 12

ABSTRACT

The Local Leo Cold Cloud (LLCC, at a distance of 11–24 pc) was studied in its relation to the Local Hot Bubble (LHB) and the result suggested that much of the observed 1/4 keV emission in that direction originates in front of the cloud. This placed a strong constraint on the distribution of X-ray emission within the LHB and called into question the assumption of a uniform distribution of X-ray emitting plasma within the Local Cavity. However, recent work has quantified the contribution of heliospheric solar wind charge exchange (SWCX) emission to the diffuse X-ray background measured by the *ROSAT* All-Sky Survey (RASS) at 1/4 keV, and led to the consistency of pressure measurements between the LHB and the local cloud component of the complex of local interstellar clouds (CLICs) surrounding the Sun. In this paper we revisit the LLCC and improve the previous analysis by using higher resolution RASS data, a serendipitous *ROSAT* pointed observation, a rigorous treatment of the band-averaged X-ray absorption cross section, and models for the heliospheric and magnetospheric SWCX contributions. We find that the foreground emission to the cloud is in excess of the expected heliospheric (interplanetary plus near Earth) SWCX contribution but that it is marginally consistent with the range of possible LHB plasma path lengths between the LLCC and the CLICs given the currently understood plasma emissivity.

Key words: ISM: bubbles – ISM: clouds – ISM: magnetic fields – solar neighborhood – X-rays: diffuse background

1. INTRODUCTION

The 1/4 keV diffuse soft-X-ray background was first observed in the late 1960s (Bowyer et al. 1968) and its origin has remained a topic of discussion since, with several different models for its origin being proposed and discarded over the years (see Snowden 2002). The longest lived of these models evolved into the Local Hot Bubble (LHB; e.g., Sanders et al. 1977; Tanaka & Bleeker 1977; Cox & Snowden 1986; Snowden et al. 1990a) where much of the observed 1/4 keV emission originates from a thermal plasma contained in the Local Cavity (LC, Knapp 1975) in the H I of the Galactic disk surrounding the Sun. It has an irregular extent of tens to a couple hundred parsecs. Additional observed 1/4 keV emission originates in the Galactic halo, possibly the local group of galaxies, and at cosmological distances (mainly the superposition of unresolved active galactic nuclei (AGNs)).

The exact relation between the LHB and the LC has been unclear. Absorption line studies showed the LC to be free of significant amounts of neutral gas and to have a distinct "wall" of neutral material rather than a gradual increase (Sfeir et al. 1999). The model of the LHB extent from Snowden et al. (1990a) did not require significant emission external to the LC, but there were directions in which the pathlength through the X-ray emitting region was significantly shorter than the distance to the wall of the LC (e.g., the direction of β CMa, Gry et al. 1985). For a detailed discussion of the various components of the local interstellar medium (ISM) see Frisch et al. (2011).

Although there is an apparently minor temperature gradient in the LHB plasma between the Galactic center and anticenter directions (Snowden et al. 1990b), over smaller angular scales the emission exhibits little variation in its hardness (e.g., Juda et al. 1991), despite having a factor of three variation in its intensity. The lack of variation in the hardness ratio implies that there is little absorbing neutral gas within the X-ray emitting region. From both *ROSAT* (Truemper 1982) and Wisconsin sounding rocket (McCammon et al. 1983) hardness ratios, the emission temperature is ~0.1 keV, at which temperature variations over any reasonable emission region are minimized. Such relative equilibrium also implies that the flux in any particular direction should be proportional to the pathlength through the emitting region. In addition, at this temperature the LHB can have only little emission in the 3/4 keV band. The plasma in the LHB likely originated from supernovae that occurred within the last ~10 million years (e.g., Maíz-Apellániz 2001; Smith & Cox 2001). However, sufficient time has passed since the last supernova for the plasma to cool and become dynamically relaxed.

Through the 1990s the LHB model was generally accepted even though the required thermal pressures within the LHB plasma and the complex of local interstellar clouds (CLICs, e.g., Redfield & Linsky 2008) surrounding the Sun were strongly discrepant (Jenkins 2009). Free expansion of plasma into the LC from the Loop I superbubble (Breitschwerdt & Schmutzler 1994; Breitschwerdt et al. 1996) was proposed as a way to decrease the temperature of the LHB without reducing its X-ray emission, but no significant observational support for

that model has been adduced (Sanders et al. 2001; Smith et al. 2014).

1.1. Solar Wind Charge Exchange Emission

In the 2000s, solar wind charge exchange (SWCX) was determined to contribute significantly to the 1/4 and 3/4 keV backgrounds. SWCX X-ray emission occurs when highly ionized metals in the solar wind (e.g., M- and L-shell ions in the 1/4 keV band and O^{+7} and O^{+8} in the 3/4 keV band) interact with neutral atoms and acquire an electron into an excited state that subsequently decays radiatively. In the solar system there are two sources of donor atoms that contribute to the general diffuse X-ray background, exospheric neutral hydrogen within Earth's magnetosheath (e.g., Robertson & Cravens 2003) and interstellar neutrals passing through the heliosphere (e.g., Lallement 2004b). The first source, when coupled with variations in the solar wind flux, produces significant temporal variations on timescales of hours to days. The second produces variations less dependent on the solar wind flux (the temporal variations are smoothed out by the integration of solar wind conditions along the line of sight through the solar system) but are dependent on the observation geometries relative to the flow of the neutrals through the solar system.

First identified as the source for the unexpected X-ray emission from comets (Cravens 1997), SWCX was subsequently identified (Cox 1998; Freyberg 1998; Cravens et al. 2001) as the source of an unknown contamination component designated long-term enhancements (LTEs, Snowden et al. 1995) observed during the *ROSAT* All-Sky Survey (RASS, Voges et al. 1999). Together the magnetospheric and heliospheric SWCX affect all astrophysical X-ray observations at energies less than ~1.5 keV.

Some models of the SWCX emission suggested that it could account for much of the X-ray emission observed within the Galactic plane (e.g., Lallement 2004a, 2004b) and perhaps eliminate the need for the LHB entirely (e.g., Koutroumpa et al. 2009a; Welsh & Shelton 2009). The extent to which the LHB was eliminated depended upon the X-ray band and the charge-exchange cross-sections assumed (compare Koutroumpa et al. 2009b and Robertson et al. 2009). In the 3/4 keV band, which is dominated by O VII and O VIII, the bulk of the emission could be shown to be due to charge-exchange. The 1/4 keV band, which contains most of what is expected to be LHB emission, is composed of many lines from many different ionization states of many different species, the bulk of which have very poorly known cross-sections. Thus, attempts to model the 1/4 keV band emission gave disparate results. Although charge-exchange cross-sections are still problematic, recent work has measured broad band-averaged cross-sections (Galeazzi et al. 2014), and has allowed a significantly more accurate empirical estimate for the emission and size of the LHB.

Initial attempts to remove the SWCX emission from the 1/4 keV maps suggested that the spatial distribution of the remaining LHB emission is far more compatible with the shape of the LC (Lallement 2004b), and recent work has shown that the gas pressure inferred from the remaining emission resolves the pressure problem (Snowden et al. 2014). It remains to be seen to what extent the removal of the SWCX emission changes the hardness ratio of the remaining emission, and whether the variation in the hardness ratio will be increased (Y. Uprety et al. 2015, in preparation). Rather than address the consistency of the interconnected physical issues described above, some of which are only indirectly addressed by observations, we propose in this work a simple test of the current LHB model: does it produce more emission along the line of sight to local X-ray absorbing clouds than can be accounted for by observations? If so, then addressing the more complicated issues is otiose, if not, then future work can begin with some reasonable expectation of success.

1.2. X-Ray Shadowing

The only current means for identifying the location of X-ray emitting plasmas in the Galaxy, other than emission associated with distinct objects such as discrete supernova remnants, is by shadowing studies (e.g., Snowden et al. 1994a; Wang & Yu 1995). In such studies the negative correlation between the column density of an interstellar cloud and the X-ray surface brightness is examined to separate the observed flux into foreground and background components relative to the cloud. For the study of the LHB, the 1/4 keV band is of relevance where one optical depth in the ISM is $\sim 10^{20}$ H I cm^{-2}, allowing clouds of even relatively modest column densities to be used as shadowing targets. One such study was done for the entire sky and found that there is significant foreground X-ray emission in all directions relative to the neutral ISM (Snowden et al. 2000).

Certain ISM clouds, particularly those that are nearby with known distances, have lent themselves to detailed shadowing studies with critical results. For example, the Draco Nebula demonstrated that there is considerable emission in excess of the extragalactic power law originating beyond the H I of the Galactic disk, as well as emission originating foreground to the Nebula (Burrows & Mendenhall 1991; Snowden et al. 1991). A *ROSAT* observation of the high latitude molecular cloud MBM12 (Magnani et al. 1985) was used to determine the X-ray intensity versus plasma path length scale factor for the LHB model (Snowden et al. 1993; Kuntz et al. 1997). Henley et al. (2007) more recently used both RASS and XMM-Newton observations of an H I filament in the southern Galactic hemisphere to study the LHB and found results relatively consistent with previous works. However, all of these studies were at the mercy of the uncertain contributions of the SWCX foreground.

One shadowing study proved to be particularly problematic for the LHB model. (Peek et al. 2011a, hereafter Paper I) examined the nearby Local Leo Cold Cloud (LLCC), which is unique in its relatively high column density (much greater than the CLICs) and its existence near the Sun within the LC. They found that while its likely distance from the Sun was between 11 and 24 pc, it still had considerable foreground X-ray emission suggesting a high emissivity for the plasma and therefore a thermal pressure far in excess of that of the CLICs.

1.3. Recent Advances

In the last year there has been a significant advance in our knowledge of 1/4 keV SWCX emission from the heliosphere. Using a sounding rocket experiment flying 1970's instrumentation (originally used for the Wisconsin survey, McCammon et al. 1983) with the required large solid-angle effective-area product (Galeazzi et al. 2011), Galeazzi et al. (2014) were able to quantify the contribution of heliospheric SWCX to the 1/4 keV RASS map, and by modeling to other observations of the 1/4 keV diffuse X-ray background. They found that ~40% of

the nearby emission in Galactic plane, a region of low surface brightness, previously attributed to the LHB originated as SWCX emission. Given this new result, it is time to revisit the LLCC analysis.

1.4. The Use of the 1/4 keV Band

The presentation in this paper is limited to the 1/4 keV background for several reasons. First, the temperature of the LHB plasma is relatively low at $T \sim 0.1$ keV so the emission is primarily in the 1/4 keV band, although a small amount of O VII emission is expected. Second, because absorption cross sections at 3/4 keV are roughly an order of magnitude smaller than at 1/4 keV, the LLCC is too thin to cast a shadow in the higher energy band, particularly considering the limited statistics of the RASS, and even the pointed observation. In addition, the smaller cross sections allow emission of distant origin (the Galactic disk, halo, and beyond) to more easily cause confusion. Third, the SWCX in the 3/4 keV band is considerably more problematic due to the dependence on a very limited number of ions, mainly O^{+7} and O^{+8}, with large temporal variations in their abundances that are not correlated with solar wind flux. As noted above, SWCX at 1/4 keV is produced by a large number of L- and M-shell lines, and empirically the variations in their solar wind abundances tend to average out (Kuntz et al. 2015). Fourth, the available X-ray data were obtained with instruments that have very low sensitivity in the 0.284–0.5 keV band excluding the use of C emission lines which could be quite interesting. In short, the LHB emission at 3/4 keV is too weak and the backgrounds are too high and variable for the higher energy band to be useful. While there has been extensive recent work concerning SWCX, it has in general been done using modern observatories which do not have usable responses at 1/4 keV. So, while the results are certainly of interest, they tend to not be particularly relevant for the purposes of this study.

In Section 2 of this paper we describe the data and RASS shadowing analysis, both of the LLCC itself and over the broader field. In Section 3 we analyze the *ROSAT* pointed observation and in Section 4 we calculate the SWCX contribution to the observed 1/4 keV emission. We discuss our results in Section 5 and present our conclusions in Section 6.

2. DATA AND RASS SHADOWING ANALYSIS

2.1. LLCC H I

The LLCC H I column density map (Figure 1 upper left panel) used in this analysis is identical to the map in Paper I. We provide here a short description of this map and note the extensive discussion of the data and data reduction contained in Paper I and references therein. The data were originally collected as part of the GALFA-HI survey, and released as part of data release 1 (Peek et al. 2011b). The GALFA HI survey, conducted on the Arecibo 305 m telescope with the ALFA instrument, has an angular resolution of 4′ and a spectral resolution equivalent to 184 m s^{-1}. Most of the map has an rms noise of 0.17 K over the 184 m s^{-1} channel, with some areas as high as 0.36 K. To find the column density the effects of H I opacity were taken into account as the cloud is quite cold (17 K).

To create the map of the LLCC used in Paper I and here, the GALFA spectra were fit pixel by pixel with the best fit of three models selected: a model of an optically thin Gaussian, a model of two optically thin Gaussians, or a model with two Gaussians, in which the more distant component is considered to be optically thin, and the closer component is considered optically thick and capable of absorbing radiation from the more distant one. (The rationale for these models and the precise methods for fitting them are discussed in significant detail in Paper 1.) The line centroids attributed to the LLCC are from a very limited range of velocities: 2–4 km s^{-1} in the LSR frame and the velocity width of the lines is ∼1 km s^{-1}.

2.2. Planck Reddening Data and LAB $N_{\rm H}$

The distant components of the X-ray background are modulated by the entire Galactic absorbing column, which includes molecular as well as neutral material. Ideally this absorbing column should be measured at the same angular resolution as the X-ray data. The Leiden/Argentina/Bonn 21 cm survey (LAB, a merging the Leiden/Dwingeloo Survey, Hartmann & Burton 1997, and the Instituto Argentino de Radioastronomía Survey, Arnal et al. 2000; Bajaja et al. 2005) is the most accurate all-sky mapping of the Galactic H I but has a resolution of ∼30′, compared to the intrinsic RASS resolution of a few arc minutes. The molecular gas has been measured by a survey of CO emission (Dame et al. 2001) that has an angular resolution of ∼15′, but there is the complication of sparse coverage at high Galactic latitudes and the conversion to a column density of H I. We therefore use the higher angular resolution (∼5′) Planck reddening map (Planck Collaboration et al. 2014) to trace the absorbing column. Assuming that the hydrogen nucleon to dust ratio remains constant, the Planck map can be scaled to the total hydrogen column density by determining the correlation between the Planck $E(B-V)$ and the total column density of H I where the total column is low enough that any molecular component is insignificant. We used the LAB survey data from the velocity range $|v| < 250$ km s^{-1}.

Figure 1 (upper right and lower left panels) shows the two data sets for the same region of the sky as the LLCC image. Figure 2 shows a scatter plot of the two data sets after binning into 32′ × 32′ bins. While there is considerable scatter in the data (at least partially related to the mismatch between the angular scale of the apparent structure indicated by the Planck reddening data and the angular resolution of the LAB survey), they do show the expected linear correlation at lower column densities along with the deviation at higher columns as the reddening data pick up the existence of molecular gas along the line of sight. From fitting the low column density data ($E(B-V) < 0.04$) in Figure 2, we find a scaling relation of $N_{\rm H} = -0.38 + 81.9 \times E(B-V)$, where $N_{\rm H}$ is in units of 10^{20} cm^{-2}. The negative offset is not expected (e.g., Peek 2013; Liszt 2014) as it implies that at low column densities there is interstellar material causing reddening that is not associated with neutral hydrogen. However, in the case of Liszt (2014), an upper cutoff of $E(B-V) = 0.07$ was used for the correlation analysis which for the LLCC region would be clearly inappropriate (see Figure 2), and would lead to a fitted relation tilted to a smaller slope and more positive offset. On the other hand, metals associated with the Galactic distribution of warm ionized gas, the Reynolds Layer (Reynolds 1989), provide additional absorption of roughly the magnitude of that which is not sampled by the 21 cm observations.

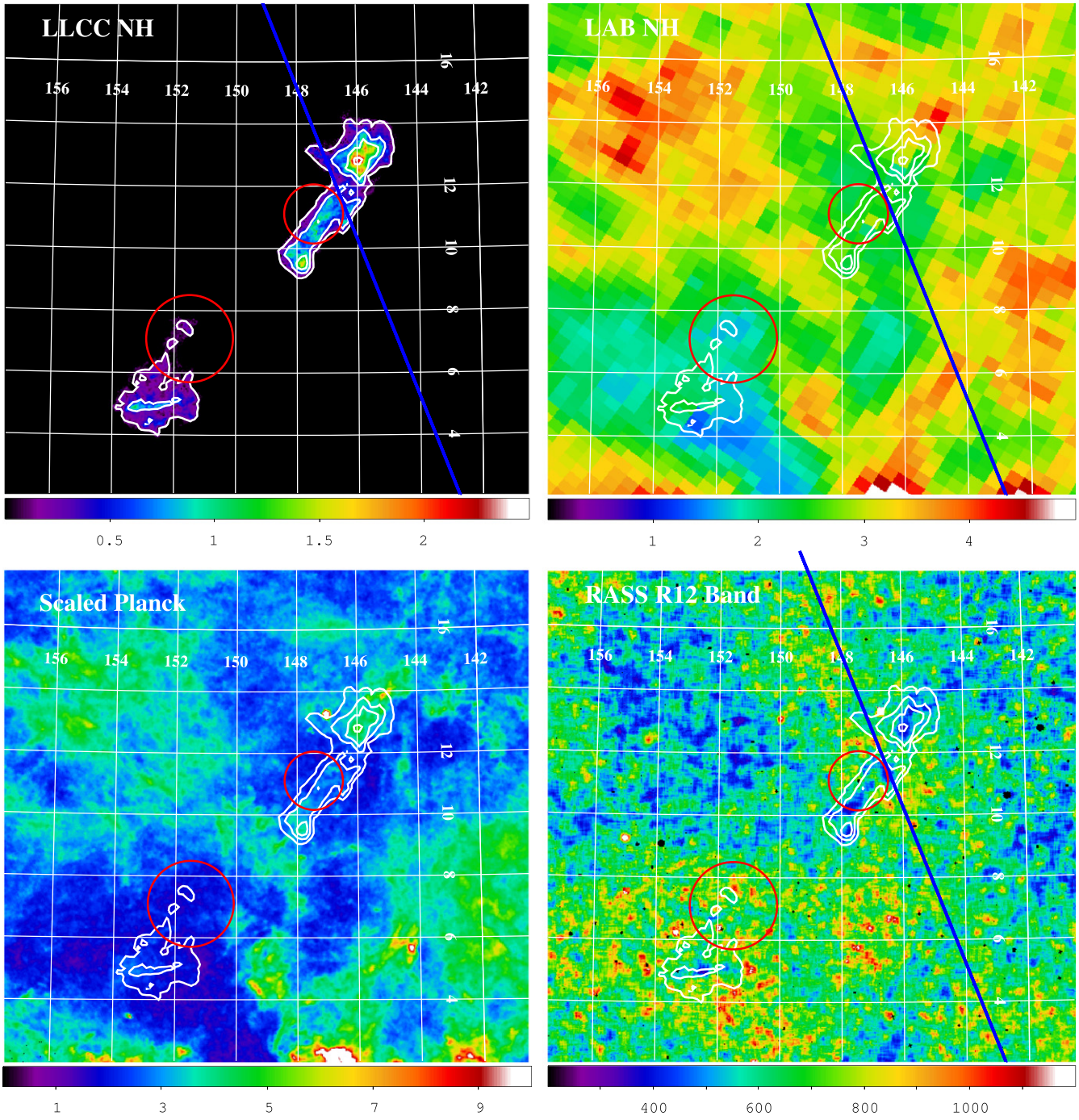

Figure 1. (Upper left) H I column density of the LLCC (Section 2.1) with the color bar in units of 10^{20} cm^{-2}. The upper red circle shows the solid angle covered by the *ROSAT* pointed observation (Section 3) while the lower red circle shows the region of the extracted RASS spectrum (Section 2.4.2). (Upper right) H I column density of the region from the LAB survey with the color bar in units of 10^{20} cm^{-2}. (Lower left) scaled Planck reddening $E(B-V)$ image of the region with the color bar in units of 10^{20} cm^{-2}. (Lower right) smoothed RASS R12 band data of the region with the color bar in RU (*ROSAT* units, 10^{-6} counts s^{-1} arcmin^{-2}). The blue line indicates the region of possible residual *ROSAT* contamination and is parallel to the survey scan direction. All fields cover the same region and the contours outline the denser parts of the LLCC. The coordinate grid is in equatorial coordinates.

2.3. RASS

The RASS data have the advantage of covering the entire field of the LLCC, and the disadvantage of relatively poor counting statistics. Paper I relied on the standard 1/4 keV survey maps which have $12' \times 12'$ pixels with roughly 10%–15% errors from counting statistics (Snowden et al. 1997). For the analysis in this paper we chose to use images with $2' \times 2'$ pixels (roughly matching the RASS average angular resolution) that are subsequently binned by the H I column density. This binning allows a better response to the finer angular structure visible in the H I data of the LLCC and the Planck reddening data.

Figure 1 (lower right) shows the RASS R12 band data binned into $2' \times 2'$ pixels and then adaptively smoothed. The R12 band covers the energy range 0.08–0.284 keV, and is also known as the 1/4 keV band or the C band, for the carbon Kα absorption edge defining the upper energy cutoff at 0.284 keV.

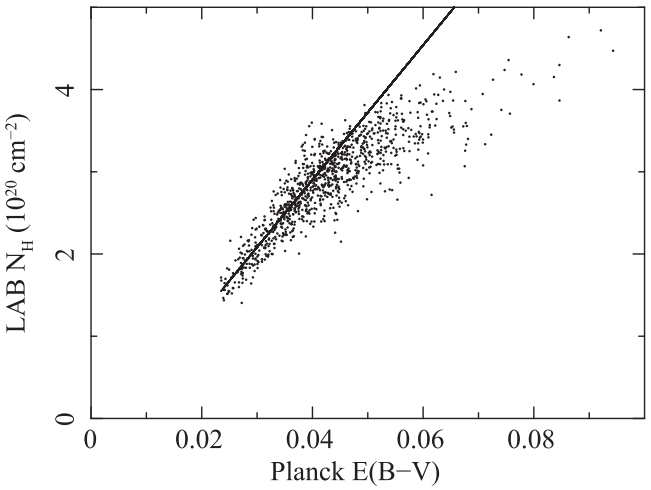

Figure 2. Scatter plot of LAB NH vs. the Planck $E(B-V)$ data. The first order polynomial fit was restricted to reddening values <0.04. The result is the relation $N_H = -0.38 + 81.9 \times E(B-V)$ (where N_H is in units of 10^{20} cm^{-2}).

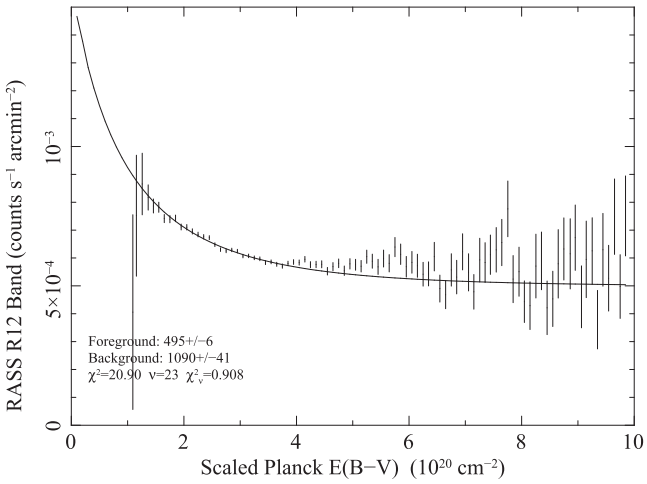

Figure 3. Scatter plot of RASS R12 band surface brightness vs. the Planck reddening data scaled to units of H I column density (see the text for details). The data have been binned in steps of 0.1×10^{20} cm^{-2} and the fit has been restricted to columns $<3.7 \times 10^{20}$ cm^{-2}.

It is clear from the data that there are strong variations in surface brightness over the field that have no relation to the LLCC. There is also the indication of a stripe of residual contamination running diagonally through the northern part of the LLCC. The stripe is parallel to the scan direction of the RASS (tilted slightly left of vertical) and is also a region of low RASS exposure. Note that the stripe is an artifact of the RASS survey geometry and data reduction that only affects the map. Indeed, there are other regions of residual contamination (striping) in the maps but they are separate from, and have no implications for other observations of that (or any other) direction on the sky. Both the variation and contamination can considerably complicate a shadowing analysis, and are likely a partial cause of the differences in results discussed below.

2.4. Shadow Analysis

2.4.1. Full-field Shadowing Analysis

In a classical shadow analysis (e.g., Burrows & Mendenhall 1991) it is assumed that there is a cloud that shadows a uniform background emission, and that there is uniform emission in front of the cloud as well. The case of LLCC is a bit more complicated as the cloud is thought to be embedded within the hot plasma of the LHB, and the more distant background emission is modulated by the Galactic H I along the entire line of sight. Therefore, besides characterizing the column density distribution of the LLCC, we must also characterize the emission from beyond the LHB and the absorption that modulates it.

To begin, we use the 1/4 keV RASS map and the LAB-scaled Planck map of the absorbing column density to investigate the variation over the field of Figure 1, and to determine the magnitude of the flux foreground to the Galactic H I. We excluded the region covered by the LLCC and did a simple shadowing analysis using the total absorbing column density. We fit the data with the function $I = I_l + I_d \times e^{-N_{HG} \times \sigma(N_{HG})}$, where I_l is the foreground intensity (relative to the Galactic absorption, N_{HG}) comprised of LHB and SWCX emission and I_d is the unabsorbed background intensity. The transmission of the Galactic H I (measured by the Planck data), $e^{-N_{HG} \times \sigma(N_{HG})}$, was parametrized by using the spectral fitting program Xspec[8] (Arnaud 1996) to absorb a 0.1 keV spectrum. While this is a simplification of the true spectrum that also includes emission from a higher temperature plasma as well as from a power law, it is acceptable for this initial fit as the range in column densities is sufficient to provide a reasonable estimate for the magnitude of the foreground emission (to be used in Section 2.4.2).

The fit result is complicated with a tight absorption correlation for column densities $<3.7 \times 10^{20}$ cm^{-2} (as shown in Figure 3 where only data with N_H less than that level were included in the fit). Above that column density there is, on average, little further fall-off of the X-ray surface brightness with increasing absorption column density until an H I column density of $N_H \sim 5.6 \times 10^{20}$ cm^{-2} is reached. However, the LLCC lies in a direction with a off-cloud Galactic absorbing column density of $N_H \sim 2.3 \times 10^{20}$ cm^{-2} placing it in a region well fit by the shadowing analysis indicating that the fitted foreground flux of $I_l = 495 \pm 6$ RU (*ROSAT* units, 10^{-6} counts s^{-1} arcmin^{-2}) is reasonable for the purposes of this paper. The fitted background flux is $I_d = 1090 \pm 31$ RU. Note that the quoted errors here and below are determined by stepping the parameter values to find the range for $\chi^2 < \chi^2_{min} + 1$. (See Table 1 for a list showing these fitted intensities along with those derived below.)

Figure 4 shows the deviations between the smoothed R12 band map and the absorption model predictions. Away from the discrepant regions, mostly in the lower right area of the field (ignoring the stripe of assumed residual contamination), the data and model agree reasonably well, suggesting that both the foreground emission (presumed to originate within the LHB) and the background emission (presumed to originate in the Galactic halo beyond the H I of the Galactic disk and as extragalactic emission) are relatively constant over the field.

2.4.2. RASS Spectral Analysis

We fit a model for the diffuse X-ray background to the RASS data from a low column density region near the southern part of the LLCC in order to determine thespectral components

[8] http://heasarc.gsfc.nasa.gov/docs/xanadu/xspec/index.html

Table 1
Fitted Parameters

Analysis	Component	Observed (RU)	Unabsorbed (RU)
Full Field	Local Emission – I_l	495 ± 6	…
…	Distant Emission – I_d	…	1090 ± 31
Spectral	Local Emission – I_l	495[a]	…
…	Distant Cooler – I_d^c	…	789 ± 72
…	Distant Hotter – I_d^h	…	68 ± 18
…	Distant Power Law – I_d^p	…	242 ± 16
…	Distant Total[b] – I_d	154 ± 11	1099 ± 76
…	Distant Total[c] – I_d	223 ± 15	1099 ± 76
RASS LLCC	LLCC Foreground – I_0	309 ± 20	…
…	LLCC LHB Background – I_1	…	233 ± 22
…	Off Cloud – $I_1 + I_d^a$	387 ± 25	…
…	Off Cloud – $I_0 + I_1 + I_d^a$	696 ± 33	…
Paper I LLCC	LLCC Foreground – I_0	398 ± 38	…
…	LLCC Background – $I_1 + I_d^a$	310 ± 40	…
…	Off Cloud – $I_0 + I_1 + I_d^a$	708 ± 11	…
Pointed LLCC	LLCC Foreground[d] – I_0	241 ± 14	…
…	LLCC LHB Background[d] – I_1	…	183 ± 20
…	LLCC Foreground[e]– I_0	264 ± 18	…
…	LLCC LHB Background[e] – I_1	…	201 ± 22
…	Off Cloud Total[e] – $I_0 + I_1 + I_d^a$	688 ± 32	…

[a] Fixed value for fit.
[b] For a Galactic H I column of 2.58×10^{20} cm^{-2}.
[c] For a Galactic H I column of 2.12×10^{20} cm^{-2}.
[d] R1L2 band.
[e] R12 band.

of the distant emission. These spectral components are then folded through the absorption of the Galactic and LLCC H I for the shadow analysis that we use to derive the parameters of the LHB and SWCX emission. The region is circular with a radius of 1.°4 centered on α, $\delta = 151.°5, 7.°1$ with an average column density of $N_{\rm HG} = 2.02 \times 10^{20}$ cm^{-2} (see Figures 1 and 4). While the region includes a small area of the LLCC, the contributed absorption is negligible when averaged over the field. Specifically, we model the observed spectrum in the following manner: an unabsorbed thermal component representing the sum of the LHB and SWCX emission (temperature allowed to float), an absorbed thermal component representing the cooler X-ray emitting halo (normalization allowed to float but the temperature fixed at a typical value of 0.1 keV), an absorbed thermal component representing the hotter X-ray emitting halo (normalization and temperature allowed to float), and an absorbed power law (normalization allowed to float with a fixed index of 1.46, Moretti et al. 2009) component representing the sum of unresolved AGN. The absorption was fixed to the Galactic value. We fit the data iteratively, varying the normalization of the unabsorbed component until achieving parameters which produced the best fit where the unabsorbed component produced the intensity determined from the full-field shadowing analysis (Section 2.4.1, $I_l = 495$ RU). Fixing this value is necessary as the relatively poor proportional counter spectral resolution allows power to be shifted between foreground and background components. The fits were done

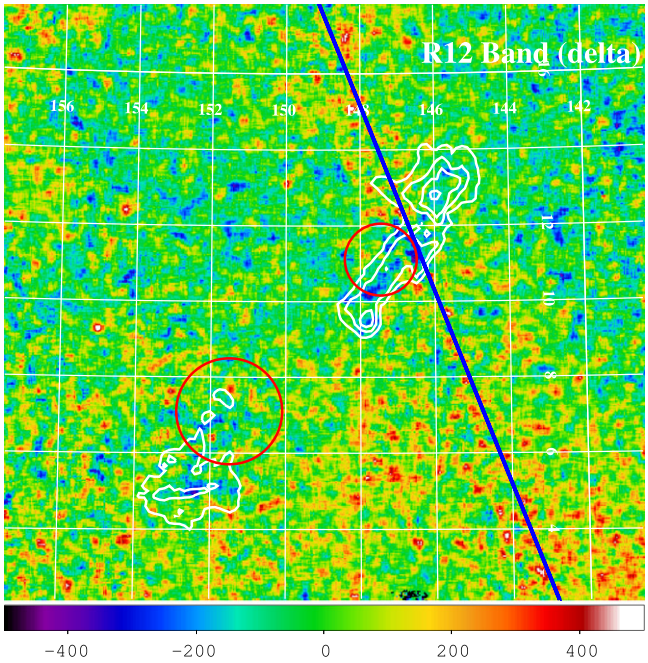

Figure 4. Difference between RASS R12 data and the fitted absorption model with the color bar in RU. The strongest positive deviations are in the lower right of the image with fainter enhancements along the bottom and the left. Note the diagonal stripe passing through the northern part of the LLCC (indicated by the blue line) as evidence for residual contamination in the RASS data. Also note that the LLCC shows up slightly as a negative deviation.

using Xspec and APEC thermal emission models with Anders & Grevesse (1989) solar abundances and Balucinska-Church & McCammon (1992) and Yan et al. (1998) absorption cross sections.

The fitted model (see Figure 5) values were $T \sim 0.105$ keV for the unabsorbed component, $T \sim 0.302$ keV for the hotter halo component, and normalizations which produced intensities of $I_l = 495$ RU for the SWCX plus LHB, $I_d^c = 789 \pm 72$ RU for the distant cooler halo component, $I_d^h = 68 \pm 18$ RU for the distant hotter halo component, and $I_d^p = 242 \pm 16$ RU for the distant power-law component. The intensities for the distant components are before any absorption and they sum to a total of $I_d = 1099 \pm 76$ RU, in good agreement with the distant flux from the shadowing measurement (1090 ± 31 RU). After absorption in the direction of the LLCC (an average column density of $N_{\rm HG} = 2.58 \times 10^{20}$ cm^{-2}) the three components provide a transmitted flux of $I_d^a = 154 \pm 11$ RU.(The superscript "a" indicates that the value is after absorption by the ISM.) We used Xspec again to parametrize the contribution of this transmitted distant spectrum (I_d^a) after absorption by the LLCC column densities for the analysis below.

2.4.3. RASS LLCC Shadowing Analysis

Using limited regions surrounding the two LLCC components we did a shadowing analysis of the RASS data using absorption by the H I map of the LLCC (see Figure 6). The full shadowing model that we use is given by Equation (1):

$$I = I_0 + I_1 \times e^{-N_{\rm HL} \times \sigma(N_{\rm HL})} + \left(I_d^c + I_d^h + I_d^p\right) \times e^{-N_{\rm HG} \times \sigma(N_{\rm HG})} \times e^{-N_{\rm HL} \times \sigma(N_{\rm HL})} \quad (1)$$

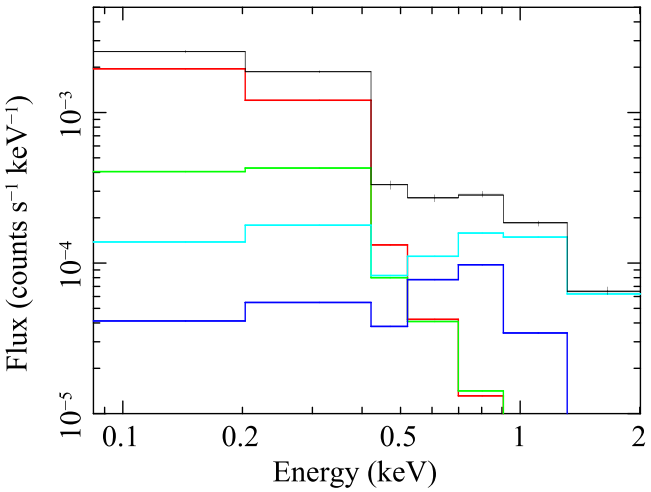

Figure 5. Spectral fit of the RASS data toward a low NH region in the field (see the text for details). The relative contributions of the four components are shown with the LHB and SWCX contribution in red, the cooler halo contribution in green, ht hotter halo contribution in dark blue, and the power-law contribution in light blue.

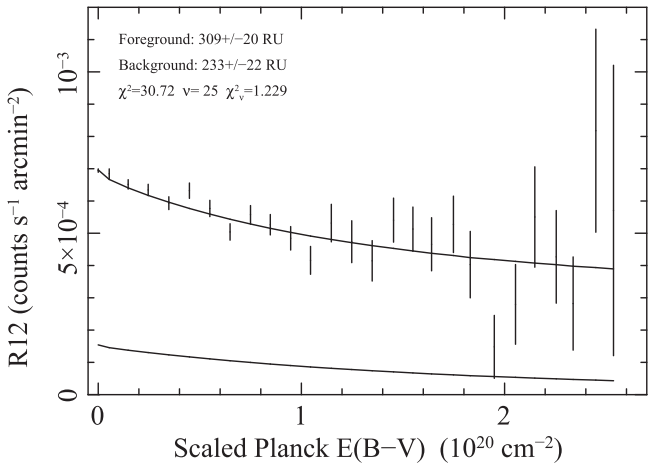

Figure 6. Scatter plot of the RASS R12 band surface brightness vs. the LLCC column density. The data have been binned in steps of 0.1×10^{20} cm^{-2}. The lower curve shows the model emission contributed by sources beyond the total Galactic column density, $\Phi(N_{\rm HL})$ (Equation (5)).

where the subscripts "0" and "1" indicate the SWCX plus LHB intensity originating in front of the LLCC and the LHB emission originating behind the LLCC, respectively. The local emission originating in front of the Galactic H I, I_l in Section 2.4.1, is the sum of I_0 and I_1. The superscripts "c," "h," and "p" again indicate the cooler X-ray emitting halo, the hotter X-ray emitting halo, and power-law components of the distant emission and have the values derived in Section 2.4.2. $N_{\rm HG}$ and $N_{\rm HL}$ are the Galactic and LLCC H I column densities. The X-ray band average effective cross section, $\sigma(N_{\rm HG})$ and $\sigma(N_{\rm HL})$, is dependent on the shape of the incident spectrum as well as the absorption column density.

Before fitting the data we subtracted the contribution of the distant component:

$$I_d^a = \left(I_d^c + I_d^h + I_d^p\right) \times e^{-N_{\rm HG}\times\sigma(N_{\rm HG})} \quad (2)$$

transmitted through the LLCC using the parametrization determined above. In other words, we folded the $I_d^a = 154$ RU of the absorbed distant emission through the additional column density of the LLCC by column density bin, and subtracted that transmitted intensity from the RASS fluxes for the bin before the shadowing analysis fitting. Equation (1) then simplifies to

$$I = I_0 + I_1 \times e^{-N_{\rm HL}\times\sigma(N_{\rm HL})} + \Phi_(N_{\rm HL}) \quad (3)$$

and then

$$I' = I - \Phi(N_{\rm HL}) = I_0 + I_1 \times e^{-N_{\rm HL}\times\sigma(N_{\rm HL})}, \quad (4)$$

where

$$\Phi(N_{\rm HL}) = I_d^a \times e^{-N_{\rm HL}\times\sigma(N_{\rm HL})}. \quad (5)$$

I' is the observed intensity after the contribution of the flux of distant origin, $\Phi(N_{\rm HL})$ (including absorption by both the Galactic and LLCC H I), is subtracted from the data. (Note the implicit assumption that the Galactic H I gas has a uniform column density over the region covered by the LLCC. This is, of course, a simplification but given that the LLCC does not completely register in the Planck data (compare the upper and lower left panels in Figure 1) the separation of the two components is not feasible. However, it is a limitation of this analysis and increases the systematic error.

The fitted value for the foreground emission (relative to the LLCC) is $I_0 = 309 \pm 20$ RU and the LHB background emission is $I_1 = 233 \pm 22$ RU ($I_1 + I_d^a = 387 \pm 25$ RU), yielding a total off-cloud flux of $I_0 + I_1 + I_d^a = 696 \pm 33$ RU. These compare to Paper I foreground and background values of $I_0 = 398 \pm 38$ RU and $I_1 + I_d^a = 310 \pm 40$ RU, and a total off-cloud intensity of $I_0 + I_1 + I_d^a = 708 \pm 11$ RU. The primary reasons for the lower foreground and higher background intensities in this work are the use of the band-average absorption cross section which is dependent on the absorption column density and the treatment of the more distant flux as an already partially absorbed spectrum. With absorption the transmitted spectrum becomes harder leading to a smaller effective absorption cross section for further absorption, which allows more of the original spectrum to be transmitted. Thus when fitting an absorption curve over a limited range of column densities using correct band-averaged cross sections, a larger fraction of the emission will be attributed to the distant component and less to the foreground component.

3. *ROSAT* POINTED OBSERVATION

Serendipitously, there is a *ROSAT* pointed observation (RP200595N00) that overlaps an area of the northern part of the LLCC (see Table 2 for the observation details), though unfortunately not its highest column density region. This pointed observation was not used in Paper I. The primary purpose of the observation was to study the star HD85091, and the star, while being relatively bright in X-rays, does not require the masking of a significant area of the detector. The data were processed using the *ROSAT* ESAS software[9] following the standard methods for studying the extended sources and the diffuse background (Snowden et al. 1994b). As the data were acquired after the gain change in the PSPC, the

[9] ftp://legacy.gsfc.nasa.gov/rosat/software/fortran/sxrb/cookbook.ps

Table 2
Pointed Observation Parameters

Parameter	Value
ObsID	RP200595N00
Date	1991 Nov 21–25
Direction	
$\alpha, \delta = 147.^{\circ}45, 11.^{\circ}1$, $l, b = 224.^{\circ}47, 44.^{\circ}50$	Survey Date[a] 1990 Nov 8–10

[a] Time period when the LLCC region was observed during the RASS.

slightly harder R1L2 band rather than the R12 band was used (0.12–0.284 keV instead of 0.08–0.284 keV). We excluded point sources and created the surface brightness image shown in Figure 7. Figure 7 also shows an image of the LLCC for the same region. For the shadowing analysis a slightly larger region surrounding the central star was excluded.

Our analysis is similar to that used for the RASS data except for the complication of using the R1L2 band rather than the R12 band. We binned the X-ray data by LLCC column density and fit for foreground and background (relative to the LLCC) intensities after subtracting fixed transmitted intensities from the distant emission (halo and extragalactic flux initially absorbed by a column density of $N_{\rm H} = 2.12 \times 10^{20}\,{\rm cm}^{-2}$ for a R1L2 bandvalue of $I_d^a = 213$ RU), with the result shown in Figure 8. Note that because the pointed observation covers a much more limited region than used in the RASS analysis, the use of the average value of $2.12 \times 10^{20}\,{\rm cm}^{-2}$ for the absorption of the distant flux is reasonable.

The data are well fit with foreground and background values of $I_0 = 241 \pm 16$ RU and $I_{\rm l} = 183 \pm 20$ RU, respectively. For a thermal plasma at $T \sim 10^{6.05}$ K, consistent with the observed spectrum in this region, the R12 to R1L2 band ratio is ~1.097 so we scale foreground and background values to $I_0 = 264 \pm 18$ RU and $I_{\rm l} = 201 \pm 22$ RU. The R12 bandvalue for the distant component is $I_d^a = 223 \pm 15$ RU, for a total off-cloud R12 band surface brightness of $I_0 + I_{\rm l} + I_d^a = 688 \pm 32$ RU. The fitted value for the foreground emission is significantly lower than that derived from the RASS data using the entire LLCC region ($I_0 = 309 \pm 20$ RU). This is likely due to two reasons. First, the pointed observation data have much better statistics, albeit over a smaller region and range in $N_{\rm H}$. The higher count density allows a higher effective angular resolution. Poorer angular resolution decreases the contrast of the shadows and artificially increases the measured foreground emission. Second, the probable residual contamination in the RASS data would act as an additional foreground component. However, the region covered by the full pointed observation lies mostly outside of the contamination stripe (most obvious in Figure 4) and has an average R1L2 band intensity of $I = 568 \pm 4$ RU, scaling to $I = 623 \pm 4$ RU in the R12 band while the RASS data for the same region have an average intensity of $I = 612 \pm 14$ RU, in good agreement. It is also possible that the use of the fixed column density for absorbing the distant flux for the RASS analysis could contribute to the difference. For all of these reasons we continue the LLCC analysis using the parameters derived from the pointed observation.

4. SWCX ANALYSIS

From Section 3, going outward from Earth we have $I_0 = 264 \pm 18$ RU of unabsorbed emission foreground to the LLCC comprised of LHB and SWCX, $I_{\rm l} = 201 \pm 22$ RU of LHB emission between the LLCC and the Galactic H I, $I_d^c = 789 \pm 72$ RU from the cool Galactic halo component, $I_d^h = 68 \pm 18$ RU from the hot halo component, and $I_d^p = 242 \pm 16$ RU from the extragalactic power law (the last three are the values unabsorbed by the intervening ISM). The question now is what emission contributes to the most local component; specifically, what fraction of the emission foreground to the LLCC is from the LHB and what fraction is SWCX emission from the heliosphere and Earth's magnetosheath.

4.1. Heliospheric SWCX

From the recent results of Galeazzi et al. (2014) we have a means of determining the SWCX X-ray emission from the heliosphere for the time periods of the X-ray observations (near solar maximum). Their paper quotes the percentage of SWCX contribution for different assumptions for the direction ($l, b \sim 144^{\circ}, 0^{\circ}$) of the minimum surface brightness of the 1/4 keV SXRB (333 RU) along their scan path, which we list as intensities in Table 3. The values for the heliospheric emission in the direction of $l, b \sim 144^{\circ}, 0^{\circ}$ can be scaled to the LLCC direction by comparing our model predictions. The estimates are calculated using a model developed by Koutroumpa et al. (2006), which in turn is based on classical hot model calculations of the interstellar neutral distributions within the solar system from Lallement et al. (1985a, 1985b, 2004).

We define a parameter κ that is proportional to the heliospheric SWCX intensity. $\kappa = \beta \int n_{\rm H} R^{-2}\, dr + \int n_{\rm He} R^{-2}\, dr = \beta \kappa_{\rm H} + \kappa_{\rm He}$, where the integral is along the line of sight through the heliosphere, $n_{\rm H}$ and $n_{\rm He}$ are the space densities of interstellar hydrogen and helium flowing through the solar system, β is the SWCX production efficiency ratio between H and He (likely in the range of 1–2), and R is the distance from the Sun. The factor of R^{-2} accounts for the dilution of the solar wind as it flows out from the Sun through the heliosphere. With the assumption that the solar wind flux flows uniformly out from the Sun, the SWCX from different directions can be determined from this simple scaling. As these observations occurred during solar maximum we are able to ignore the variation of the solar wind flux as a function of solar latitude as the slow wind extends from the ecliptic plane to the poles. We also assume that as both observations (RASS and pointed observation) occurred during solar maximum that the average solar wind fluxes for the two time periods were similar. In addition, as the line of sight integral samples several weeks of solar wind conditions (the solar wind travels 1 AU in ~4 days), the variation of the solar wind is considerably smoothed supporting the above assumption.

With $n_{\rm H}$ and $n_{\rm He}$ in units of ${\rm cm}^{-3}$ and R and dr in units of AU, the units of κ are ${\rm cm}^{-3}\,{\rm AU}^{-1}$. The integrals for the $l, b \sim 144^{\circ}, 0^{\circ}$ direction during the survey were $\kappa_{\rm H}^1 = 0.006103\ {\rm cm}^{-3}\,{\rm AU}^{-1}$ and $\kappa_{\rm He}^1 = 0.01873\ {\rm cm}^{-3}\,{\rm AU}^{-1}$ while the integrals for the LLCC direction ($l, b \sim 224.^{\circ}5, 44.^{\circ}5$) at the time of the pointed observation are $\kappa_{\rm H}^2 = 0.008596\ {\rm cm}^{-3}\,{\rm AU}^{-1}$ and $\kappa_{\rm He}^2 = 0.03071\ {\rm cm}^{-3}\,{\rm AU}^{-1}$, respectively. The heliospheric

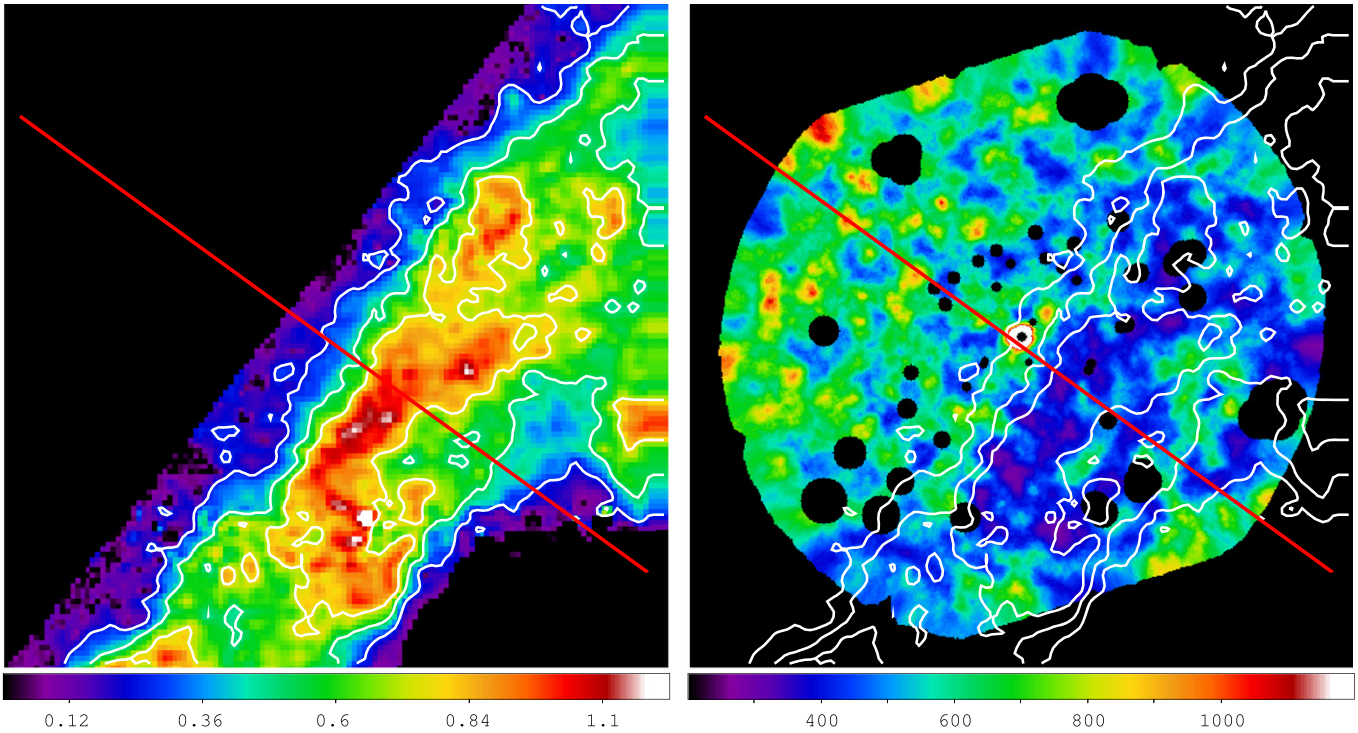

Figure 7. (Right) *ROSAT* pointed observation image of a region of the northern part of the LLCC in the R1L2 band in RU. The contours are of the LLCC H I and are the same as in the left-hand figure. The diagonal red line in both images shows the cut direction used in the limb-brightening analysis of Section 5.3. The angular scale for both images is the same with the *ROSAT* data spanning ~2°. (Left) H I column density for the same region of the northern part of the LLCC as the *ROSAT* pointed observation, with units of 10^{20} cm^{-2}.

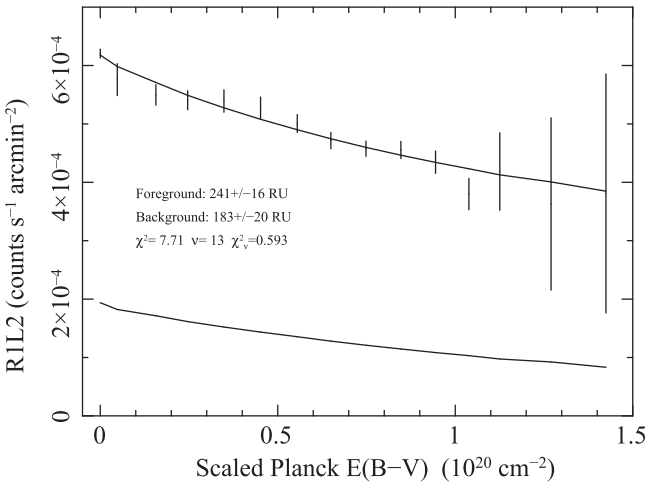

Figure 8. Scatter plot of pointed observation R1L2 band surface brightness vs. the LLCC column density. The data have been binned in steps of 0.1 × 10^{20} cm^{-2}.

SWCX scale factor between the two directions is then $(\kappa^2_{\rm He} + \beta\kappa^2_{\rm H})/(\kappa^1_{\rm He} + \beta\kappa^1_{\rm H})$.

For the scaling we consider the four assumptions of Galeazzi et al. (2014) listed in their Table 1. Namely, that there is or is not a residual 50 RU of magnetosheath SWCX contribution in the RASS and that the relative efficiency for SWCX X-ray production between H and He is either 1 or 2. With the different assumptions there is a range of 116 RU to 206 RU in predicted SWCX X-ray flux from the interaction with interstellar neutrals in the heliosphere that are listed in Table 3.

Table 3
ROSAT Pointed Observation Parameters

Parameter	Value[a]	Value[a]	Value[a]	Value[a]
SWCX[b]	130 ± 20	123 ± 27	130 ± 13	140 ± 20
MS[c]	0	50	0	50
HS[d]	130	73	130	90
$\beta = \alpha_{\rm H}/\alpha_{\rm He}$ [e]	1×	1×	2×	2×
LLCC HS[f]	206	116	202	140
LLCC MS[g]	66	66	66	66
LLCC HS+MS[h]	272	182	268	206

[a] Units of RU in the R12 band.
[b] Total SWCX emission in the direction of $l, b \sim 224°.5, 44°.5$ for the various assumptions. The values were derived by multiplying the measured RASS R12 band flux of 333 RU by the percentage SWCX contribution listed in their Table 1 in RU.
[c] Assumed residual magnetosheath SWCX contribution to the RASS data in the direction of $l, b \sim 144°, 0°$ in RU.
[d] Heliospheric SWCX contribution to the RASS data in the direction of $l, b \sim 144°, 0°$ in RU.
[e] Ratio of the hydrogen to helium charge exchange X-ray emission efficiency.
[f] RASS heliospheric SWCX emission scaled to the LLCC observation in RU.
[g] LLCC observation magnetosheath SWCX emission in RU.
[h] Total LLCC SWCX emission in RU.

4.2. Magnetosheath SWCX

In Galeazzi et al. (2014) the value of 50 RU for the residual magnetosheath SWCX emission in the RASS 1/4 keV band was essentially an educated guess using the correlation between solar wind flux and LTE intensity shown in Cravens et al. (2001). However, for the *ROSAT* pointed observation

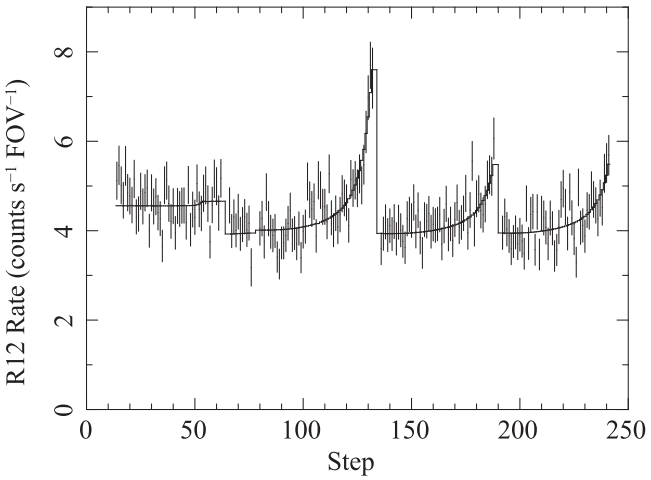

Figure 9. R1L2 band light curve of the pointed observation. Each step is 30 s and the gaps between observation intervals have been compressed. The narrow peaks in the count rate are due to scattered solar X-rays.

considered here, we are able to improve on that assumption based on the correlation between solar wind flux and 1/4 keV LTE intensity demonstrated in Cravens et al. (2001) and Kuntz et al. (2015). Figure 9 shows the R1L2 band light curve (count rate) for the pointed observation while Figure 10 shows the IMP-8 (Frank et al. 1976) measured solar wind proton flux for the observation time interval (obtained through the OMNIWeb Service, King & Papitashvili 2005).

Interpolating the solar wind flux where necessary, Figure 11 shows a scatter plot of the solar wind and SWCX plus SXRB data with the best-fit linear model (the *ROSAT* counts due to scattered solar X-rays and the particle background have been removed). The ESAS LTE modeling process cleans the *ROSAT* data to the level of the minimum count rate, 3.83 counts s^{-1} for this observation. Assuming a constant scaling between solar wind flux and the magnetosheath SWCX 1/4 keV flux over the period of the observation and extrapolating the fit down to zero solar wind flux leaves a count rate of 3.42 counts s^{-1}. This implies a residual magnetosheath SWCX count rate of 0.41 counts s^{-1} over the full field of view. From Snowden et al. (1995), the scale factor between counts s^{-1} over the FOV and the 0.12–0.49 keV band count rate in RU is 148. The rate must be scaled to the R12 band (an increase of 5.4%) and scaled for the smaller detector area used in the R1L2 band (the vetoing along two edges of the PSPC was less efficient at lower gain, an increase of 2.3%) for a total scaling of ~1.08. This increases the model magnetosheath SWCX to 160 RU (counts s^{-1})$^{-1}$ (the scaling is relatively insensitive to the exact spectral shape as the poor spectral resolution of proportional counters smears the events so broadly). This implies a residual R12 band magnetosheath SWCX rate of 66 RU. The model magnetosheath SWCX component has been added to the heliospheric component in the last row of Table 3 for the total SWCX contribution to the observation.

5. DISCUSSION

5.1. Distribution of Emission within the LHB

With the assumption that both the RASS and the pointed observation have the specified residual magnetosheath SWCX emission, this leaves us with a likely range of heliospheric plus magnetosheath SWCX emission contribution to the pointed

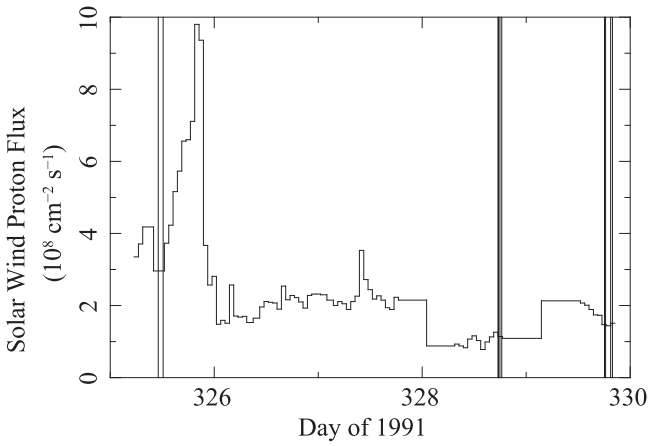

Figure 10. IMP-8 solar wind flux for the time period of the pointed observation. The vertical bars show the observation intervals.

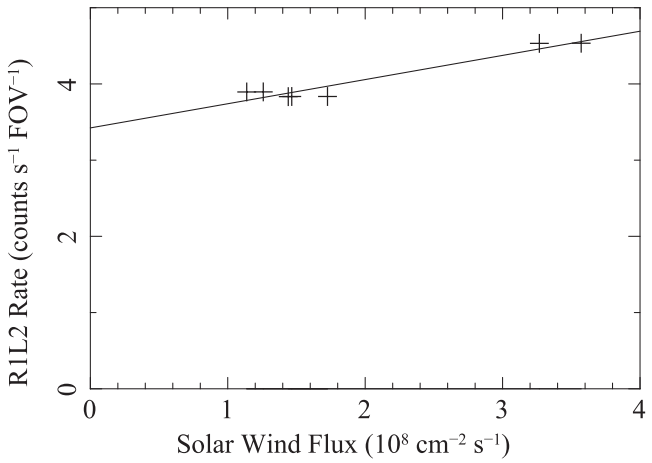

Figure 11. Scatter plot and best-fit relation between the IMP-8 solar wind flux and the R1L2 band flux for the time period of the pointed observation.

observation data of 182–206 RU (columns 3 and 5 in Table 3). The final R12 band picture within the LHB is then $I_0^{\rm SWCX} = 194 \pm 12$ RU (using the range of values as an estimate of the uncertainties) of SWCX emission, $I_0^{\rm LHB} = 70 \pm 22$ RU of LHB emission foreground to the LLCC, and $I_{\rm l} = 201 \pm 22$ RU of LHB emission from between the LLCC and the edge of the LC (or at least the end of the emitting plasma along the line of sight foreground to the absorbing H I).

From Redfield & Falcoon (2008) and Linsky & Redfield (2014) the LLCC is near but not overlapping the Mic, Gem, and Leo members of the CLICs that have distance upper limits of 5.1, 6.7, and 11.1 pc, respectively. However, they are relatively close on the sky so we will use their distance limits to provide an estimate of 5–11 pc for the extent of the CLICs in the LLCC direction that we assume excludes the X-ray emitting plasma of the LHB. The results of Paper I place the LLCC probably between 11.3 and 24.3 pc from the Sun, leaving 0–19 pc of path length foreground to the LLCC for the LHB plasma. From the results of Snowden et al. (2014), the emissivity of the plasma in the LHB is 2.4 ± 0.5 RU pc^{-1} (noting that this value was well matched by the value of 2.5 RU pc^{-1} based on a LHB and LC geometric argument in Puspitarini et al. 2014), suggesting that the $I_0^{\rm LHB} = 70 \pm 22$ RU of foreground LHB emission requires a path length of

$D_0^{\rm LHB} = 29 \pm 11$ pc, consistent with the available path length at $\sim 1.5\sigma$. We note, however, that the uncertainty for $I_0^{\rm LHB}$ and therefore $D_0^{\rm LHB}$ are very conservative as the systematic uncertainties for the estimation of the SWCX contribution are unknown, and therefore not included.

5.2. The Extent of the LHB

Again using the X-ray emissivity from Snowden et al. (2014), the path length required for the $I^{\rm LHB} = 271 \pm 31$ RU of LHB emission is $D^{\rm LHB} = 113 \pm 28$ pc. Adding on the path length within the CLICs (8 ± 3 pc) leads to a minimum distance to the edge of the LC of 121 ± 28 pc, noting again that the edge of the plasma need not be coincident with edge of the LC, only foreground to it. Unfortunately at the relatively high Galactic latitude of $b \sim 45°$ for the LLCC there are limited numbers of stars appropriate for constraining the location of the neutral ISM and the H I clouds are relatively diffuse. Thus it is difficult to exactly locate the edge of the LC. However, Meyer et al. (2006) place the distance to the first neutral material beyond the LLCC at 100–150 pc, likely allowing space for the required LHB emission path length.

5.3. Emission from the LLCC/Hot Plasma Interface

It has long been postulated that there should be enhanced X-ray emission from the interface regions between cooler neutral clouds and any hot plasma surrounding the cloud (e.g., Slavin 1989). As the cloud loses material by evaporation into the plasma that is then heated there should be a density enhancement within the plasma resulting in a greater emissivity. While such emission is thought to have been observed (e.g., Miyata & Tsunemi 2001; Andersson et al. 2004), it is associated with hotter plasmas and younger, more active supernova remnants or stellar wind bubbles. Conclusive observational evidence from the LHB, a region of cooler plasma and relaxed conditions, supporting this phenomenon is lacking. However, the LLCC provides a near perfect test case for such emission as it is an apparently isolated cloud floating in the hot plasma of the LHB. Figure 12 shows the R12 band count rate for a cut through the LLCC perpendicular to the roughly straight edge covered by the pointed observation (see Figure 7) for both the pointed observation and RASS data (to improve the RASS statistics a larger region was used). The pointed observation shows no indication of limb brightening for the region covered, up to $\sim 50'$ from the edge (~ 0.3 pc). The RASS data with their greater coverage show no limb brightening over two widths of the cloud. In the case of possible thermal emission this suggests that either there is no emission from the interface region or that it occurs at a lower effective temperature where the *ROSAT* data are insensitive. In the case of charge exchange emission, this suggests that there is insufficient donor material reaching the hot plasma from cloud to cause a significant enhancement in the observed R12 flux.

6. CONCLUSIONS

This paper has presented a reanalysis of LLCC data in relation to the LHB using higher resolution RASS data, a serendipitous *ROSAT* pointed observation, Planck $E(B-V)$ and LAB NH data, models for SWCX X-ray emission, and a rigorous treatment of the band-average absorption of X-ray spectra. We find that Paper I overestimated the amount of X-ray emission foreground to the LLCC due to limitations in the RASS data and a simple treatment of the absorption cross section, and that the bulk of the foreground emission is heliospheric and magnetosheath SWCX in origin. These results suggest that the LLCC data are not in significant contradiction to the LHB model for the local ISM and 1/4 keV diffuse background.

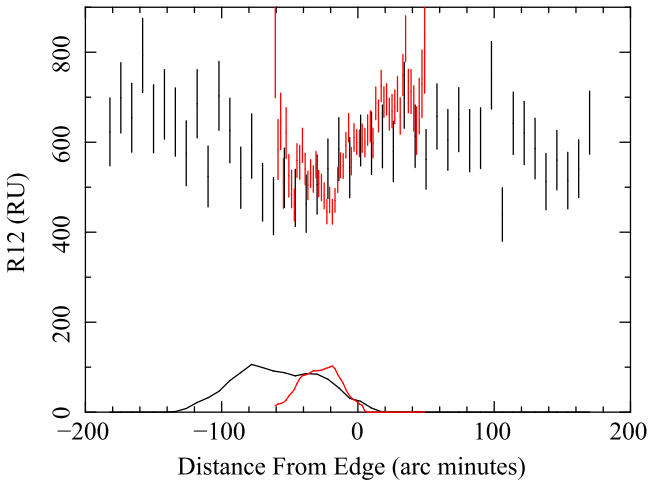

Figure 12. Count rate profile running perpendicular to the northern edge of the LLCC covered by the pointed observation (the trajectory note in Figure 7). Red indicates data from the pointed observation while black indicates RASS data. The lower curves show the LLCC profile (10^{18} H I cm^{-2}) with the differences between the RASS and pointed data due to the RASS covering a larger region. Positive distances from the edge of the LLCC indicate locations to the northeast.

The picture arising from this work has $I_0^{\rm SWCX} = 194 \pm 12$ RU of SWCX emission, with ~66 RU from the magnetosheath and ~128 RU from the heliosphere. The CLICs extend 8 ± 3 pc from the Sun with the LLCC at a distance of 11–24 pc. There is $I_0^{\rm LHB} = 70 \pm 22$ RU of LHB emission foreground to the LLCC requiring a path length of $D_0^{\rm LHB} = 29 \pm 11$ pc of emission, fitting into the <19 pc of available path length foreground to the LLCC at the $\sim 1.5\sigma$ level. There is $I_1 = 201 \pm 22$ RU of emission between the LLCC and the edge of the LC requiring a path length of $D_1 = 84 \pm 17$ pc, for a total path length of LHB emission of $D^{\rm LHB} = 113 \pm 28$ pc, or 121 ± 28 pc to the edge of the LHB from the Sun when the path length within the CLICs is added. This is a lower limit to the edge of the LC in this direction. Beyond the H I of the Galactic disk there is an additional $I_d^c = 789 \pm 72$ RU from the cool Galactic halo component, $I_d^h = 68 \pm 18$ RU from the hot halo component, and $I_d^p = 242 \pm 16$ RU from the extragalactic power law, again in this specific direction. Finally, we find no evidence for significant limb brightening from the interface region between the LLCC and the surrounding plasma.

S.L.S. would like to thank the l'Observatoire de Paris—Meudon GEPI for their hospitality and support as much of the analysis in this paper took place while he was a Visiting Scientist in 2014 October–November. D.K. and R.L. would like to acknowledge financial support from the French National Program "Physique Chimie du Milieu Interstellaire" of the Institut National des Sciences de l'Univers (INSU). The *ROSAT* PSPC data used in the LLCC analysis were acquired from the HEASARC archive. The IMP-8 data were obtained from the GSFC/SPDF OMNIWeb interface at http://omniweb.gsfc.nasa.gov.

REFERENCES

Anders, E., & Grevesse, N. 1989, GeCoA, 53, 197
Andersson, B.-G., Knauth, D. C., Snowden, S. L., Shelton, R. L., & Wannier, P. G. 2004, ApJ, 606, 341
Arnal, E. M., Bajaja, E., Larrarte, J. J., Morras, R., & Pöppel, W. G. L. 2000, A&AS, 142, 35
Arnaud, K. A. 1996, in ASP Conf. Ser. 101, Astronomical Data Analysis Software and Systems V, ed. G. H. Jacoby, & J. Barnes (San Francisco, CA: ASP), 17
Bajaja, E., Arnal, E. M., Larrarte, J. J., et al. 2005, A&A, 440, 767
Balucinska-Church, M., & McCammon, D. 1992, ApJ, 400, 699
Bowyer, C. S., Field, G. B., & Mack, J. E. 1968, Natur, 217, 32
Breitschwerdt, D., Egger, R., Freyberg, M. J., Frisch, P. C., & Vallerga, J. V. 1996, SSRv, 78, 183
Breitschwerdt, D., & Schmutzler, T. 1994, Natur, 371, 774
Burrows, D. N., & Mendenhall, J. A. 1991, Natur, 351, 629
Cox, D. P. 1998, in IAU Colloq. 166, The Local Bubble and Beyond, ed. D. Breitschwerdt, M. J. Freyberg, & J. Truemper (Berlin: Springer), 121
Cox, D. P., & Snowden, S. L. 1986, AdSpR, 6, 97
Cravens, T. E. 1997, GeoRL, 24, 105
Cravens, T. E., Robertson, I. P., & Snowden, S. L. 2001, JGR, 106, 24883
Dame, T. M., Hartmann, D., & Thaddeus, P. 2001, ApJ, 547, 792
Frank, L. A., Ackerson, K. L., & Lepping, R. P. 1976, JGR, 81, 5859
Freyberg, M. J. 1998, in IAU Colloq. 166, The Local Bubble and Beyond, ed. D. Breitschwerdt, M. J. Freyberg, & J. Truemper (Berlin: Springer), 113
Frisch, P. C., Redfield, S., & Slavin, J. D. 2011, ARA&A, 49, 237
Galeazzi, M., Chiao, M., Collier, M. R., et al. 2011, ExA, 32, 83
Galeazzi, M., Chiao, M., & Collier, M. R. 2014, Natur, 512, 171
Gry, C., York, D. G., & Vidal-Madjar, A. 1985, ApJ, 296, 593
Hartmann, D., & Burton, W. B. 1997, Atlas of Galactic Neutral Hydrogen (Cambridge: Cambridge Univ. Pess)
Henley, D. B., Shelton, R. L., & Kuntz, K. D. 2007, ApJ, 661, 304
Jenkins, E. B. 2009, SSRv, 143, 205
Juda, M., Bloch, J. J., Edwards, B. C., et al. 1991, ApJ, 367, 182
King, J. H., & Papitashvili, N. E. 2005, JGRA, 110, 2104
Knapp, G. R. 1975, AJ, 80, 111
Koutroumpa, D., Collier, M. R., Kuntz, K. D., Lallement, R., & Snowden, S. L. 2009a, ApJ, 697, 1214
Koutroumpa, D., Lallement, R., & Kharchenko, V. 2009b, in AIP Conf. Ser. 1156, The Local Bubble and Beyond II, ed. R. K. Smith, S. L. Snowden, & K. D. Kuntz (Melville, NY: AIP), 62
Koutroumpa, D., Lallement, R., Kharchenko, V., et al. 2006, A&A, 460, 289
Kuntz, K. D., Collado-Vega, Y. M., Collier, M. R., et al. 2015, arXiv:1503.04756
Kuntz, K. D., Snowden, S. L., & Verter, F. 1997, ApJ, 484, 245
Lallement, R. 2004a, A&A, 422, 391
Lallement, R. 2004b, A&A, 418, 143
Lallement, R., Bertaux, J. L., & Dalaudier, F. 1985a, A&A, 150, 21
Lallement, R., Bertaux, J. L., & Kurt, V. G. 1985b, JGR, 90, 1413
Lallement, R., Raymond, J. C., Vallerga, J., et al. 2004, A&A, 426, 875
Linsky, J. L., & Redfield, S. 2014, Ap&SS, 354, 29
Liszt, H. 2014, ApJ, 783, 17
Magnani, L., Blitz, L., & Mundy, L. 1985, ApJ, 295, 402
Maíz-Apellániz, J. 2001, ApJL, 560, L83
McCammon, D., Burrows, D. N., Sanders, W. T., & Kraushaar, W. L. 1983, ApJ, 269, 107
Meyer, D. M., Lauroesch, J. T., Heiles, C., Peek, J. E. G., & Engelhorn, K. 2006, ApJL, 650, L67
Miyata, E., & Tsunemi, H. 2001, ApJ, 552, 624
Moretti, A., Pagani, C., Cusumano, G., et al. 2009, A&A, 493, 501
Peek, J. E. G. 2013, ApJL, 766, L6
Peek, J. E. G., Heiles, C., Peek, K. M. G., Meyer, D. M., & Lauroesch, J. T. 2011a, ApJ, 735, 129 (Paper I)
Peek, J. E. G., Heiles, C., Douglas, K. A., et al. 2011b, ApJS, 194, 20
Planck Collaboration, Abergel, A., Ade, P. A. R., et al. 2014, A&A, 571, A11
Puspitarini, L., Lallement, R., Vergely, J. L., & Snowden, S. L. 2014, arXiv:1401.6899
Redfield, S., & Falcon, R. E. 2008, ApJ, 683, 207
Redfield, S., & Linsky, J. L. 2008, ApJ, 673, 283
Reynolds, R. J. 1989, ApJL, 339, L29
Robertson, I. P., & Cravens, T. E. 2003, GeoRL, 30, 1439
Robertson, I. P., Kuntz, K. D., Collier, M. R., Cravens, T. E., & Snowden, S. L. 2009, AIP Conf. Ser. 1156, The Local Bubble and Beyond II, ed. R. K. Smith, S. L. Snowden, & K. D. Kuntz (Melville, NY: AIP), 52
Sanders, W. T., Edgar, R. J., Kraushaar, W. L., McCammon, D., & Morgenthaler, J. P. 2001, ApJ, 554, 694
Sanders, W. T., Kraushaar, W. L., Nousek, J. A., & Fried, P. M. 1977, ApJL, 217, L87
Sfeir, D. M., Lallement, R., Crifo, F., & Welsh, B. Y. 1999, A&A, 346, 785
Slavin, J. D. 1989, ApJ, 346, 718
Smith, R. K., & Cox, D. P. 2001, ApJS, 134, 283
Smith, R. K., Foster, A. R., Edgar, R. J., & Brickhouse, N. S. 2014, ApJ, 787, 77
Snowden, S. L. 2002, in The Hot Part of the Interstellar Medium, ed. J. A. Bleeker, J. Geiss, & M. C. E. Huber (Dordrecht: Kluwer), 581
Snowden, S. L., Chiao, M., Collier, M. R., et al. 2014, ApJL, 791, L14
Snowden, S. L., Cox, D. P., McCammon, D., & Sanders, W. T. 1990a, ApJ, 354, 211
Snowden, S. L., Egger, R., Freyberg, M. J., et al. 1997, ApJ, 485, 125
Snowden, S. L., Freyberg, M. J., Kuntz, K. D., & Sanders, W. T. 2000, ApJS, 128, 171
Snowden, S. L., Freyberg, M. J., Plucinsky, P. P., et al. 1995, ApJ, 454, 643
Snowden, S. L., Hasinger, G., Jahoda, K., et al. 1994a, ApJ, 430, 601
Snowden, S. L., McCammon, D., Burrows, D. N., & Mendenhall, J. A. 1994b, ApJ, 424, 714
Snowden, S. L., McCammon, D., & Verter, F. 1993, ApJL, 409, L21
Snowden, S. L., Mebold, U., Hirth, W., Herbstmeier, U., & Schmitt, J. H. M. 1991, Sci, 252, 1529
Snowden, S. L., Schmitt, J. H. M. M., & Edwards, B. C. 1990b, ApJ, 364, 118
Tanaka, Y., & Bleeker, J. A. M. 1977, SSRv, 20, 815
Truemper, J. 1982, AdSpR, 2, 241
Voges, W., Aschenbach, B., Boller, T., et al. 1999, A&A, 349, 389
Wang, Q. D., & Yu, K. C. 1995, AJ, 109, 698
Welsh, B. Y., & Shelton, R. L. 2009, Ap&SS, 323, 1
Yan, M., Sadeghpour, H. R., & Dalgarno, A. 1998, ApJ, 496, 1044